



# Satellite-based global monitoring of urban-scale methane emissions

Huihui Long<sup>1</sup>, Maria Tsvilidou<sup>1</sup>, Hugo Ricketts<sup>1,2</sup>, and Grant Allen<sup>1</sup>

<sup>1</sup>Department of Earth & Environmental Science, Simon Building, University of Manchester, Manchester M13 9PL, UK

<sup>2</sup>National Centre for Atmospheric Science, University of Manchester, Oxford Road, Manchester M13 9PL, United Kingdom

**Correspondence:** Grant Allen ([grant.allen@manchester.ac.uk](mailto:grant.allen@manchester.ac.uk))

**Abstract.** Quantifying and understanding methane emissions of cities are of great importance given their role in current and future mitigation efforts to combat climate changing emissions. However, it remains challenging to routinely and accurately characterize and verify city-scale methane emission inventories. Previous studies of urban methane emissions have employed a range of emission quantification methods, leading to inconsistent estimates and different associated uncertainties. As a result, a robust and widely applicable framework for quantifying urban emissions remains lacking. In this study, we describe our development of an advanced mass balance emissions accounting using TROPOspheric Monitoring Instrument (TROPOMI) satellite observations to estimate the orbit-level net bulk (city-level) methane emissions and corresponding emissions uncertainties due to the method. We have tested and demonstrated that the novel integration of hourly-resolved wind data under the planetary boundary layer (PBL) enables a more conceptually-accurate assessment of methane emissions from urban areas than methods that do not consider thermodynamic variability. In addition, we have introduced an upwind-based approach for background determination, in which background methane concentrations were defined using city-adjacent regions along the PBL-pressure-weighted-mean upwind direction. Initial assessments with this approach were tested for three megacities (London, Los Angeles and New York) between 2021 and 2023. Results indicate that existing emission inventories generally underestimate urban methane emissions across all three cities, but with significant inter-annual and inter-city variability. Satellite-derived emissions from 2021 to 2023 range from 5.99 to 11.90  $\text{t h}^{-1}$  in London, 26.21 to 62.77  $\text{t h}^{-1}$  in Los Angeles, and 30.85 to 44.77  $\text{t h}^{-1}$  in New York, corresponding to factors of approximately 0.1-2.0, 0.3-2.1, and 5.1-9.2 times the inventory estimates, respectively. Compared with previous top-down urban studies for the same cities, our emission estimates are generally lower but remain broadly consistent when differences in urban extent are taken into account. These results demonstrate that satellite observations can facilitate ongoing city-scale emission quantification, support inventory reconciliation and reporting, offer the potential for long-term monitoring globally, and further aid efforts to assess whether stated methane emission targets are being met.

## 1 Introduction

Methane ( $\text{CH}_4$ ), the second most significant greenhouse gas after carbon dioxide ( $\text{CO}_2$ ), is responsible for one third of the rise in global mean surface air temperature from 1750 to 2019 (Szopa et al., 2021). The relatively short atmospheric lifetime (about 9 years; Prather et al., 2012) and substantial global warming potential (almost 82 times that of  $\text{CO}_2$  over a 20-year period; IPCC, 2023) make the reduction of methane emissions a compelling strategy for tackling near-term climate change (Forster et al., 2021). All projected pathways for restricting global warming to 1.5°C above pre-industrial levels need a rapid



decrease in methane emissions (IPCC, 2023). Over 150 countries have committed to reducing their methane emissions across all sectors by a minimum of 30% below 2020 levels by 2030, via their respective Nationally Determined Contributions to the Paris Agreement and the Global Methane Pledge (Global Methane Pledge, 2023).

30 Methane is released through many natural (e.g., wetlands, inland freshwaters, etc.) and processes, but about 65% (range of 63-68%) of it originates from human activities, which include agriculture, waste management, and fossil fuel production and use (Saunois et al., 2025). Large emission uncertainties (between 20-35%) have been identified across these sectors in terms of average annual magnitudes and trends among different global bottom-up inventories (Tibrewal et al., 2024). These disagreements primarily arise from differences in input data (e.g., activity data and emission factors), as well as variations in  
35 sectoral coverage and times-series gap-filling strategies (Saunois et al., 2017; Tibrewal et al., 2024). Urban areas are large and spatially-concentrated methane emission sources, which may impede climate goals, given the prevalent use of natural gas (He et al., 2019), pipeline gas leaks due to aging infrastructure (Weller et al., 2020), and wastewater treatment systems (Defratyka et al., 2021). Field studies quantifying methane emissions in urban areas have found that official bottom-up inventories can underestimate methane emissions by a factor of 2 to 3 (Anderson et al., 2021; Pitt et al., 2022; Plant et al., 2019). Such discrep-  
40 ancies imply that there are substantial unexplained urban sources of methane (Saint-Vincent and Pekney, 2019). Monitoring and mitigation efforts are urgently required, as more than half of the global population already resides in urban areas; this proportion is projected to rise to 70% by 2050 (United Nations Department of Economic and Social Affairs, 2025), which is expected to exacerbate landfill and wastewater emissions (U.S. Environmental Protection Agency, 2019).

Top-down (measurement-led) quantification methods can evaluate emissions in urban areas from unidentified or underes-  
45 timated sources, in contrast to bottom-up inventories, which rely on activity data and emission factors that are often difficult to define accurately. Many top-down studies have employed in situ observations (Schiferl et al., 2025), mobile and vehicle ground monitors (Maazallahi et al., 2020), or aircraft (Allen et al., 2019; Pitt et al., 2022) to infer total methane emissions in urban regions. These approaches can deliver accurate emissions snapshots, but cannot deliver continuous temporal monitor-  
50 ing and may have restricted spatial sensitivity. Considering the spatial extent of urban area methane emissions across nations and globally, satellite-based instruments with high spatial resolution have been shown to have the potential to provide implementable monitoring solutions (Cooper et al., 2022; Shen et al., 2023; Vanselow et al., 2024). In 2023, de Foy et al. (2023) demonstrated that satellite column concentration from TROPospheric Monitoring Instrument (TROPOMI) can be used as actual emissions to constrain current urban-scale methane inventories based on significant methane enhancements over 61  
55 urban areas worldwide. More recently, Nesser et al. (2024) used TROPOMI data to conduct a preliminary national analysis of urban methane emissions across North America (focusing on the contiguous U.S.). However, urban methane emissions are often characterized by a total (yet ambiguous) uncertainty in prior literature, without detailed error-propagation information. Moreover, the inferred emission distributions, which depend on the characteristics of the atmospheric transport models used in different inversion systems, are not typically consistent across satellite-based and surface-measurement-based studies (Saunois et al., 2025). In poorly observed regions (e.g. India, China), where most of the global population resides, measurement-led  
60 validation of national emissions is even more challenging. This highlights the need to develop more improved methods with



greater transparency in uncertainty budgeting, in order to offer more conceptually-accurate and greater confidence in emissions detection, quantification and reporting, which can be globally implemented.

In this study, we present and test new developments to the source pixel method (Buchwitz et al., 2017; Jacob et al., 2016), which we have used to quantify emissions of methane for three megacities. These developments include an improved quantifi-  
65 cation of planetary boundary layer (PBL) winds and upwind background concentration used in the method. Such improvements are more conceptually accurate than more simple source pixel methods that are agnostic to upwind background direction and wind representation throughout the depth of the PBL. We analyze single-orbit (Level-2) methane column measurements from TROPOMI to quantify urban methane enhancements relative to an upwind background for three case study cities (London, Los Angeles, and New York) over the period 2021-2023, mapped onto a regular  $0.1^\circ \times 0.1^\circ$  spatial grid. We then evaluate methane  
70 emission rates and forward-propagate systematic emission uncertainty using this improved source pixel method. To test and develop the method, we also investigated its sensitivity to varying meteorological conditions (especially wind vectors), and differences in data coverage over the urban source region.

## 2 Data and methodology

To detect emission rates in hotspot cities based on TROPOMI methane products, we applied a fast and simple oversampling  
75 method to achieve a constant spatial resolution ( $0.1^\circ \times 0.1^\circ$ ) of TROPOMI atmospheric dry-air methane column mixing ratio ( $XCH_4$ ), and then we used an improved data-driven source pixel method to further infer the emission rates of urban areas. The technical framework of our study is illustrated in Fig. 1, which shows data selection and pre-conditioning prior to emissions quantification. Section 2.1 describes data products, including satellite retrievals and data pre-processing steps to filter for high-quality observations, winds, inventory repository and our definition of urban spatial boundaries. Section 2.2 describes the  
80 oversampling process of pixel-heterogeneous Level-2 satellite data to temporally-averaged Level-3 data. Section 2.3 describes the improved source pixel method, which quantifies city-level methane emission rate for each viable (cloud-free) overpass. Section 2.4 describes the detailed uncertainty analysis for city-scale emission quantification, including both single-orbit estimates and multiple-overpass estimates across different timescales.

### 2.1 Data

#### 85 2.1.1 TROPOMI Satellite retrievals

TROPOMI serves as the only instrument onboard the polar sun-synchronous Sentinel-5 Precursor (S-5P) satellite, launched on 13 October 2017 at an altitude of 824 km, with a consistent 13:30 local overpass time (Veefkind et al., 2012). The instrument retrieves the methane column by detecting solar backscattered light in the shortwave infrared (SWIR)  $2.3 \mu\text{m}$  absorption band with near-uniform sensitivity across the troposphere.  $XCH_4$  is retrieved using a full-physics algorithm under clear-sky  
90 conditions, with daily global coverage and spatial resolution of  $7 \times 7 \text{ km}^2$  ( $7 \times 5.5 \text{ km}^2$  since August 2019) at nadir (Butz et al., 2011).

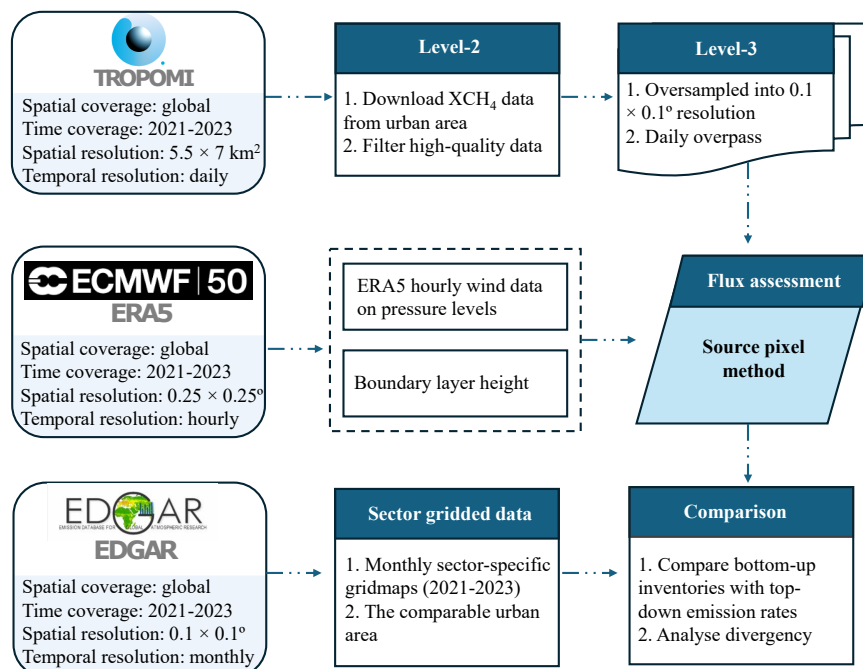


**Figure 1.** Technique framework of the improved source pixel method designed for urban area methane emissions quantification.

In this study, we have used the RemoTeC-S5P operational retrieval product of TROPOMI (Hasekamp et al., 2024). This TROPOMI XCH<sub>4</sub> product was corrected for already known retrieval biases, and validation with independent ground-based measurements from the Total Column Carbon Observing Network showed that the bias-corrected XCH<sub>4</sub> significantly improved the uncorrected product (Hasekamp et al., 2024; Hu et al., 2018). Thus, the corrected column-averaged dry-air mole fraction of methane is used in this study, and obtained at the original swath resolution from 1 January 2021 to 31 December 2023. The retrievals of methane columns achieve an effective success rate of about 3% of total daytime observations over land (cloud-free measurements), principally constrained by cloud cover, variable topography, heterogeneous albedo of coast pixels and high levels of aerosol scattering (Hasekamp et al., 2024). Thus, we only use good-quality XCH<sub>4</sub> measurements under cloud-free conditions, which we define and filter using the following metadata parameters: qa\_value (quality assurance value) > 0.5, solar zenith angle (< 70°), viewing zenith angle (< 60°), and smooth topography (1 standard deviation of surface elevation variability < 80 m within a 5 km radius). Also, pixels with a SWIR aerosol optical thickness > 0.07, or a retrieval precision > 10 ppb were removed. We further screened retrieval data using the surface classification flag recommended by Balasus et al. (2023) and de Foy et al. (2023), keeping only pixels flagged as 0 (land) and 2 (some water), and excluding inland water pixels with poor spectral fits (e.g., with a flag of 2 and SWIR chi-square > 20000) to remove artifacts. We note that some studies used the well-filtered TROPOMI WFM-DOAS XCH<sub>4</sub> product (Schneising et al., 2023) or blended TROPOMI + GOSAT product



(Balasus et al., 2023) that had passed the quality check to estimate emissions of regions (Liu et al., 2024; Wang et al., 2026). But significant differences of XCH<sub>4</sub> retrievals and spatial emission patterns from different products have been identified, which may be attributed to aerosol scattering and sensitivity to albedo (Sicsik-Paré et al., 2025). The operational product used here provides more temporally homogeneous coverage and detailed information about aerosol optical thickness and albedo, which we consider to be the most relevant parameters that may be expected to influence background methane columns, which source pixel methods can be highly sensitive to (see Sect. 2.3).

### 2.1.2 Wind data

The TROPOMI RemoTeC-S5P data product provides the horizontal components of surface wind at 10 meter height, which is derived from the European Center for Medium range Weather Forecasts (ECMWF) and interpolated in space and time to SWIR measurement to calculate the near-surface wind vector of each TROPOMI pixel. In 2019, ECMWF released the latest generation reanalysis model, ERA5, using a four-dimensional variational (4D-VAR) assimilation scheme (Hersbach et al., 2020). For the source pixel method, ERA5 offers significant advantages over 10 m wind in terms of its ability to incorporate *u* and *v* wind observations more proximal to time of measurement, and on several pressure levels through the PBL. ERA5 also provides other meteorological variables such as corresponding PBL height and pressure and temperature (from which atmospheric density can be derived). At a spatial resolution of  $0.25^\circ \times 0.25^\circ$ , ERA5 provides hourly meteorological data, enabling the probability quantification of wind uncertainty (see Sect. 2.4) by incorporating temporal variability in meteorological conditions during satellite overpasses of extensive urban areas. The PBL is the primary layer in which surface emissions are dispersed and advected over urban spatial scales. It is characterized by turbulence and convective mixing, typically mixing throughout the whole layer on timescales of advection across city scales (Pitt et al., 2019). The improved source pixel method is therefore sensitive to prevailing winds throughout the PBL (and not simply 10 m winds), and emission rate is conceptually proportional to mean PBL wind speed (as shown in Sect. 2.3). We therefore calculate total wind for each overpass as the pressure-weighted average of wind speed and direction across all ERA5 PBL pressure levels over a given urban source region, using daily ERA5 PBL height data. Compared with previous studies using prior versions of the source pixel method, we choose here to use the pressure-weighted boundary layer winds instead of 10 m wind provided in the TROPOMI retrieval products, because, conceptually, this better captures the expected ventilation across the source pixel that arises by turbulent horizontal advection in the urban PBL (Pandey et al., 2021; Varon et al., 2018).

A further comparison of 10 m wind from TROPOMI products and ERA5 data over London, Los Angeles and New York was conducted to assess sensitivity to the choice of winds in the source pixel method in general. Figure 2 indicates that there are significant differences between the 10 m wind and pressure-weighted PBL wind over the source region for the same overpasses. This was a consistent observation in all three cities and influences both the wind speed (that is directly linear to the final methane rate) and the wind direction, which is critical for determining the location of the background region assumed (see Sect. 2.3). In turn, this can affect the magnitude of the methane enhancement, and therefore the calculated emissions. For Los Angeles, most of the time, TROPOMI 10 m wind is from the north-northeast to east-northeast direction and lower than  $6 \text{ ms}^{-1}$ . But for ERA5 PBL-weighted winds, this is dominated from west-southwest to south-southwest and north to north-northwest, with



wind speeds up to  $\sim 10 \text{ ms}^{-1}$ . Wind direction discrepancies of these two datasets are less significant for London and New York, but all illustrate a higher wind speed in ERA5 (as may be expected). This directly implies a higher emission rate due to the wind ventilation of the source pixel than methods that consider only near-surface wind vector.

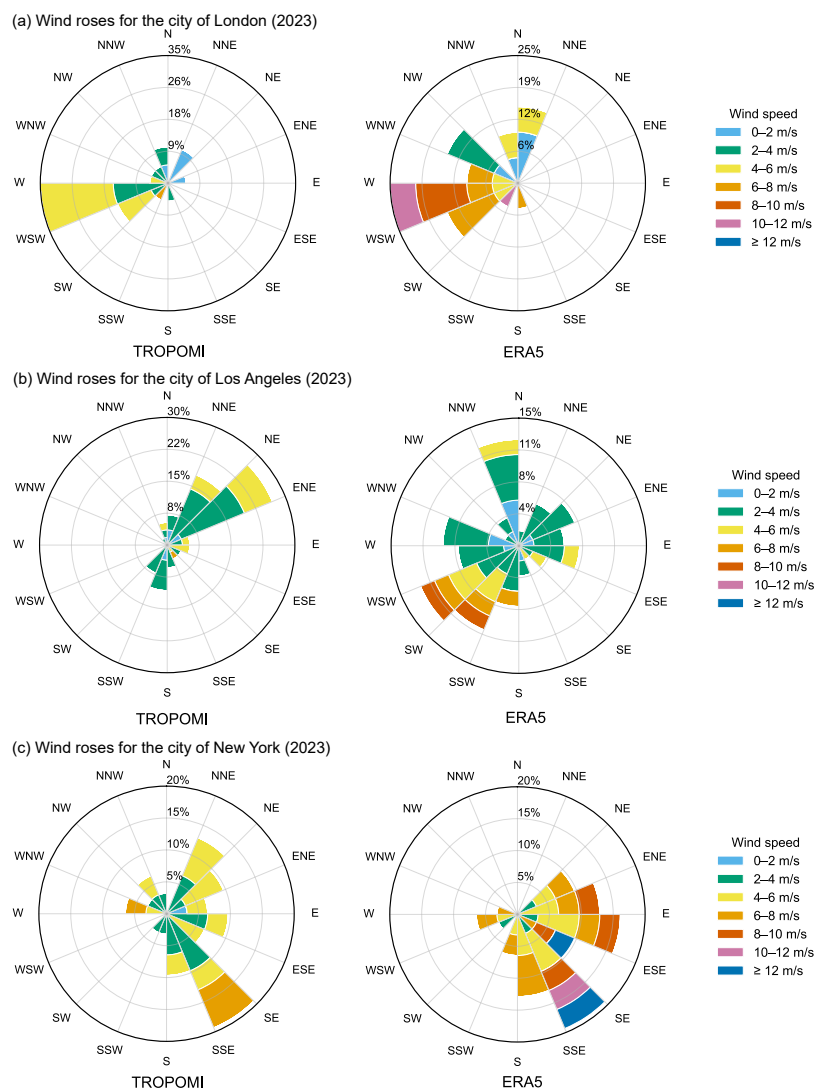


**Figure 2.** Comparison of wind roses derived from TROPOMI products and ERA5 reanalysis over London (a), Los Angeles (b) and New York (c) for 2023. The annual average wind statistics of each city are calculated using only days with valid TROPOMI overpasses, filtered by all data quality control threshold described in Sect. 2.1.1.



### 2.1.3 Emission inventories

145 To better understand the nature of any potential discrepancy between bottom-up inventories and top-down measurements, a set of inventories are used for comparison here. The Emissions Database for Global Atmospheric Research (EDGAR v8.0) provides detailed information about anthropogenic emissions of various air pollutants and greenhouse gases (Crippa et al., 2024). EDGAR compiles data from a variety of sources, allowing differentiation between individual sources in a source region. For each sector, annual and gridded emissions are provided from 1970 to 2023 with a spatial resolution of  $0.1^\circ \times 0.1^\circ$ . This  
150 enables us to scale and compare methane emissions in a specified source region with same location and area in EDGAR. Apart from the anthropogenic emissions in EDGAR, the only natural sources of methane included in this study are extracted from WetCHARTs v1.3.3 (Bloom et al., 2024). This dataset was selected because natural wetland emissions constitute the largest and most uncertain component of natural methane sources in bottom-up models and inventories (Saunio et al., 2025).

In addition to EDGAR, gridded methane emission data from the National Atmospheric Emission Inventory (NAEI) for  
155 the UK, and the U.S. Environmental Protection Agency (EPA) are also used for comparison. NAEI gives annualized gridded emissions of methane at  $1 \times 1$  km resolution from 2005 to 2023 and provides sector-specific emissions across the UK (Tsagatakis et al., 2024). The gridded EPA anthropogenic greenhouse gas inventory (GHGI) provides annual methane emissions ( $0.1^\circ \times 0.1^\circ$ ) for the contiguous United States (CONUS). The gridded GHGI v2 Express Extension product includes annual emissions from 2012 to 2020 for 27 source categories (Maasakkers et al., 2023). These gridded methane emission prod-  
160 ucts can be used to examine which inventories may perform best and to gain insights on sectors that may dominate uncertainty when compared with the emissions derived in this study at the urban scale.

### 2.1.4 Choice of urban source domain

Since urban inventories reported for climate change mitigation can be significantly influenced by the choice of city boundary, the cartographic boundary shapefiles of each case study city in this study were obtained from the official website that available  
165 to public (City of Los Angeles, 2026; Greater London Authority, 2026; New York State GIS Program Office, 2026). In the process of selecting the urban domain used as the source region in this study, an area was selected as the source region for each study using a square box centered on the mid-points of the maximal meridional and zonal extent of the city's shapefile, oriented such that two sides of the box are perpendicular to the mean PBL wind. This ensures that the full width of the emitted urban plume is observable (in principle) over the city in the TROPOMI scene (assuming cloud-free conditions).

## 170 2.2 Oversampling method

The pixel size (in terms of ground footprint) during each TROPOMI orbit are different, resulting from changing viewing angles across the swath, and Earth's curvature. In order to map Level-2 pixels to Level-3 grids as a temporal average for use in this work, such that a source region is based on a city boundary shapefile, and directly comparable to gridded bottom-up inventories, we use oversampling to generate a regularized grid. Here we have oversampled the  $XCH_4$  retrieval data from TROPOMI to  
175 a  $0.1^\circ \times 0.1^\circ$  resolution for each orbit. Oversampling makes use of shifting pixel locations and sizes in daily observations to



achieve spatial resolutions finer than the original pixel size. The oversampling method treats satellite observation pixels as surface polygons and calculates the fractional area of each grid cell covered by individual pixel polygons. The calculation of this overlapping area requires filling the irregular pixels with regular grid cells, also known as "tessellation", which is well-described by Zhu et al. (2017), and described by the following relationship:

$$180 \quad \bar{\Omega}(i) = \frac{\sum_{p=1}^{N(i)} \frac{A(p,i)}{S(p)\sigma(p)} \Omega(p)}{\sum_{p=1}^{N(i)} \frac{A(p,i)}{S(p)\sigma(p)}} \quad (1)$$

Where  $A(p,i)$  is the overlap area between the pixel  $p$  and oversampling grid cell  $i$ .  $S(p)$  is the pixel area.  $\sigma(p)$  denotes the absolute error standard deviation of the satellite observation data as reported in the retrieval products.  $\Omega(p)$  represents the corrected average total column mixing ratio of methane. Through this oversampling method, the area-weighted and error-weighted average column for each  $0.1^\circ \times 0.1^\circ$  grid cell is then derived. In order to fit to the re-gridded resolution, all variables of TROPOMI retrieval products included in this study were calculated using the same oversampling method.

### 2.3 Emission quantification method

To quantify emissions for each city, the source pixel method that was first introduced by Jacob et al. (2016) is applied here, which was further developed and fully modeled by Buchwitz et al. (2017). This fast data-driven method is derived from the concept of mass balance, and designed to calculate methane surface emissions of areas showing elevated atmospheric concentrations relative to their surrounding areas from satellite retrieval  $XCH_4$  maps. An elegant advantage of the method is that emissions can be inferred solely from methane enhancements (e.g., source minus background value) in the source pixels, along with knowledge of a representative advective flow vector (i.e. mean wind). Source pixel methods usually apply to time-averaged satellite-derived  $XCH_4$  data sets. Despite large systematic emission uncertainties (typically of the order tens of percent), emission uncertainty can be reduced when the signal (over a city) is proportionately larger than the surrounding background area (and when the background is less variable). The source pixel method was used by Buchwitz et al. (2017) to derive urban emissions with magnitudes of several  $Mt CH_4 yr^{-1}$ . Here, we propose an improved source pixel method that integrates detailed wind vector information to better represent ventilation over the source region and methane enhancement relative to the upwind background, thereby improving the quantification of city-scale methane emissions.

Detailed application of this improved method in this work is as follows: we first re-grid TROPOMI Level-2 retrieval products using a regular latitude-longitude grid (here:  $0.1^\circ \times 0.1^\circ$  resolution following oversampling as described in Sect. 2.2). The second step defines a source region (SR) and background region (BR) aligned to the mean PBL wind as described in Sect. 2.1.2. The background region refers to a region of equal area defined to be upwind of the source region. This is a novel development for this study compared with previous applications of the source pixel method, which hitherto implicitly assume that the observed methane enhancement in the source area is associated with the source area alone (with no account for the true upwind background) and that any outflow of the source region can be neglected (Buchwitz et al., 2017). Debates remain on the choice of the background domain due to different research scales and locations, including (1) expanding the coordinates of the source



region to a size defined by the maximum extents in the meridional and zonal directions (Vanselow et al., 2024), (2) using a large background region to decrease the impacts on emissions estimates from any potential emissions in the background region (Pandey et al., 2021), (3) proposing a land cover weighting method to estimate the background  $XCH_4$  (Xing et al., 2025). An alternative approach to defining a background concentration is to characterizing adjacent up-wind regions, though insufficient observations in this region may be caused by clouds, oceans, and other factors affecting retrieval quality can limit the number of days available for emissions analysis. In this work, we chose the up-wind method to define the background region located immediately-adjacent and in the upwind direction as defined by PBL-pressure-weighted mean wind as described in Sect. 2.1.2. The third step calculated the methane enhancement (e.g.  $\Delta XCH_4$ ) over the source region compared with its adjacent up-wind background region. This methane enhancement is computed by subtracting the mean retrieved  $XCH_4$  in the background region from the mean over the source region. To minimize potential bias from the statistics of small sampling (and therefore potential bias from outlier pixels remaining after data-filtering), we defined two further thresholds in data coverage that must be met in order for emissions for a city from a single orbit to be considered meaningful, as follows: the source region must be at least 25% populated with valid data after filtering (Fig.A2). and the background region must have at least 10 observations. This resulted in the loss of the majority of city overpasses (due predominantly to cloudy scenes, in addition to surrounding coasts). We assert that this is an important and necessary loss of data to preserve emissions accuracy. We noted that emissions calculated where we attempted to relax these constraints further, resulted in wildly different and simply impossible results.

Finally, combined with additional TROPOMI retrieval products, the elements extracted above provide all inputs necessary to implement the improved source pixel method and estimate urban methane emission rates:

$$E = \frac{M_{CH_4} (SR_{CH_4} - BG_{CH_4}) UPW}{M_{air} g} \quad (2)$$

where  $E$  is the emission rate of the source region with unit  $t h^{-1}$ ,  $M_{CH_4}$  denotes the molecular mass of  $CH_4$ , with a constant factor of  $0.016 \text{ kg mol}^{-1}$ ,  $M_{air}$  is the molecular mass of dry air,  $0.029 \text{ kg mol}^{-1}$ . Methane enhancement  $\Delta XCH_4$ , computed from the  $(SR_{CH_4} - BG_{CH_4})$ , is observed from a source relative to the upwind background.  $U$  is the mean PBL wind speed of the source box in  $\text{km h}^{-1}$ ,  $P$  refers to the atmospheric surface air pressure, provided with the retrieval product,  $W$  is the length of side of the square source box (unit: km),  $g$  is the acceleration of gravity ( $9.8 \text{ m s}^{-2}$ ).

An illustrative example of the improved source pixel method used in this study is shown in Fig. 3 for London, demonstrating how the retrieved methane enhancement over the source region ( $\Delta XCH_4$ ) is defined and oriented to the ERA5 wind direction and the corresponding location of the up-wind background region. To compute the PBL wind speed and direction, ERA5 hourly wind products are gridded onto the same spatial grid as TROPOMI data (Fig. 3b). After calculating the pressure-weighted average wind vector in the PBL over source region, the location of the up-wind background is obtained, as shown in Fig. 3c. Using this method, the valid orbits that pass through the satellite configuration filters, coverage threshold and uncertainty threshold, vary significantly across years and in different months. In Fig. 3d, the lowest observation is in New York city in 2021, with only 5 valid orbits that overpass the urban domain. Coverage increases to 8 and 25 overpass in 2022 and 2023, but the month-to-month variation is notable with most of the orbits observed in spring and winter seasons. Los Angeles has



240 the largest coverage, nearly 100 total single orbits are usable in the method from 2021 to 2023. The number of annual valid  
satellite overpass over London urban area are between 10 and 25 orbits, and mostly are observed in spring, summer and winter  
seasons (as might be expected due to autumn storms and cloud). Clearly, such seasonality and inter-year variability in the  
number of valid scenes can be expected to lead to bias. This would be expected to be a limitation inherent to any application  
of the source pixel method using TROPOMI, even without the additional filtering we have applied here to reduce potential for  
245 bias associated with cloudy scenes. We highlight this problem here as an honest appraisal of the challenges and limitations of  
using satellite data for urban emissions quantification. Put simply, biases implicit to sampling may remain, despite any attempt  
to minimize their presence. Therefore, when comparing annualized emissions by the improved method in this study (or any  
other) with inventories, it is important to be cognizant of how such biases may manifest; for example in the context of which  
periods of a given year may be poorly sampled compared to others and whether this may expected to manifest as a low or high  
250 bias overall versus perfect year-round sampling.

## 2.4 Emission uncertainty quantification

To estimate the uncertainty of urban emission rates, we assess the influence of uncertainties in  $\Delta XCH_4$  and  $U$ , which can be  
derived statistically from TROPOMI and ERA5 data products. This procedure captures the potential sensitivity of systematic  
errors in the retrieved column mixing ratio over source pixels and uncertainty in the background estimate used to define  
255 methane enhancements. Also, the simulation of the constant wind within source region can result in large uncertainty because  
of changes in wind direction over the course of a typical day (Varon et al., 2018).

When assessing the  $\Delta XCH_4$  uncertainty, the satellite retrieval measurements of atmospheric albedo and aerosol in SWIR  
band are involved. They may cause an overestimate or underestimate of the average column dry air mixing ratio relative to  
its real abundance through lengthening or shortening the light path (Jacob et al., 2016). To calculate the error of methane  
260 enhancement results from the albedo and aerosol difference in the source region and background region, we use a linear fitting  
method to simulate the relationship between the column methane  $XCH_4$  and the factors of albedo and aerosol within the  
source or background regions. The uncertainty of wind speed is estimated from the standard deviation of wind speed over the  
source region in a period of four consecutive hours around the TROPOMI local overpass time. Then, a representative statistical  
confidence error of emission rates  $\sigma_E$  for a single scene is computed as the sum in quadrature of  $1\sigma$  of methane enhancement  
265 and wind speed.

$$y = ax + b \quad (3)$$

$$\sigma_{\Delta XCH_4} = \sqrt{[a_{alb}(x_{SR,alb} - x_{BR,alb})]^2 + [a_{aer}(x_{SR,aer} - x_{BR,aer})]^2} \quad (4)$$

$$\sigma_E = E \cdot \sqrt{\left(\frac{\sigma_{\Delta XCH_4}}{\Delta XCH_4}\right)^2 + \left(\frac{\sigma_U}{U}\right)^2} \quad (5)$$

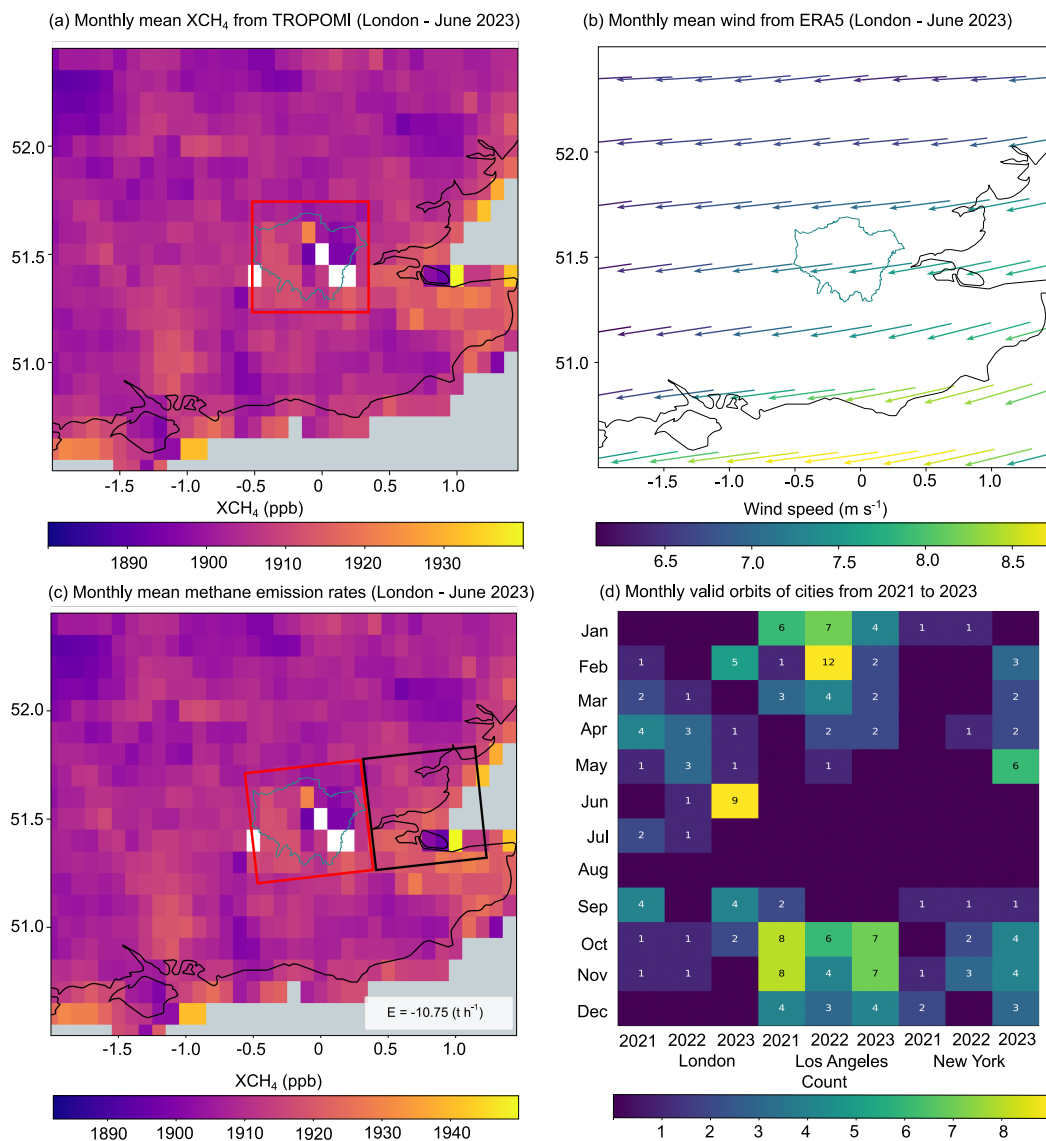


**Figure 3.** Illustration of the upwind background determination based on the improved source pixel method used in this study. (a) Mean XCH<sub>4</sub> retrievals derived from the TROPOMI instrument for London in June 2023. (b) Monthly mean wind vectors derived from hourly resolved ERA5 reanalysis data set for London in June 2023. (c) Location of the immediately adjacent upwind background region defined according to the wind direction shown in panel (b). (d) Monthly number of valid satellite overpasses for the three cities during 2021–2023 that passed strict quality control and were used in the final emission estimates.

Here,  $a_{alb}$  and  $a_{aer}$  denote the slopes of the linear regression (Eq. 3) obtained by regressing XCH<sub>4</sub> against surface albedo and aerosol optical thickness, respectively, within the study domain.  $x_{SR}$  and  $x_{BR}$  refer to the mean value of albedo or aerosol in the source region and background region.



For urban areas that have multiple valid overpasses (i.e. days), the emission rates and uncertainties need to be averaged to generate total urban estimates at the desired timescale (e.g. monthly or yearly). To ensure the quality of results, we only include orbits with uncertainties of less than 100%. While most previous studies using the source pixel method have analyzed an aggregated sets of observations through equally weighting each day in the average, we use the spatial coverage (in %) of valid observations in the source region to weight each overpass in an effort to reduce bias. Finally, the uncertainty in the temporally-averaged estimates is calculated as the root mean square error (RMSE), in Eq. 6.

$$RMSE (\%) = \frac{\sqrt{\frac{1}{N} \sum_{i=1}^N (\sigma_{E_i})^2}}{\frac{1}{N} \sum_{i=1}^N E_i} \times 100 \quad (6)$$

Where  $\sigma_{E_i}$  refers to the uncertainty of emission rate for orbit  $i$  (Eq. 5), and  $E_i$  denotes the calculated emission rate of orbit  $i$ ,  $N$  is the valid overpass of TROPOMI for a given urban domain that restricted by cloud, water, and oceans, etc.

### 3 Results

#### 3.1 Urban emissions in London

The urban domain used to implement the improved source pixel method of this work is defined over London, a source region that has been the topic of numerous methane emission studies (Helfter et al., 2016; Pitt et al., 2019). The results for 2021-2023 are summarized in Fig. 4. Figure 4a presents the spatial distribution of mean  $XCH_4$  levels over London urban area for the study period. The urban enhancement relative to the surrounding background is generally modest, with no persistently strong hotspot visible within the defined source region. The relatively weak spatial contrast implies that the calculated  $\Delta XCH_4$  is sensitive to background variability. In particular, when the upwind sector (e.g. background  $XCH_4$ ) contains elevated methane from other nearby source regions, the derived  $\Delta XCH_4$  over the study area can be substantially reduced and may occasionally become negative (see Sect. 2.3). This result is consistent with previous aircraft-based and dispersion modeling analyses over London (Pitt et al., 2019), which also reported relatively small urban-scale enhancements. The corresponding monthly time series of  $\Delta XCH_4$  of London urban area is shown in Fig. 4c. The annual mean enhancement increased from  $1.47 \pm 0.76$  ppb in 2021 to  $1.98 \pm 1.38$  ppb in 2022, before slightly declining to  $1.70 \pm 0.83$  ppb in 2023. A clear seasonal cycle is observed in the monthly average  $\Delta XCH_4$ , with larger enhancements during winter months. This seasonality likely reflects a combination of increased emissions and more stable atmospheric conditions. It should also be noted that data coverage is uneven throughout the year due to cloud contamination, which reduces the number of valid TROPOMI overpasses in certain months. Figure 4b presents estimated methane emission rates for London from 2021 to 2023, derived using the method outlined in Sect. 2.3. The three-year mean emission rate is  $7.78 \pm 4.84$   $t h^{-1}$ , where the long-term uncertainty is estimated from multiple satellite overpasses following Equation 6. The annual mean emissions are  $5.99 \pm 3.25$   $t h^{-1}$  (2021),  $11.90 \pm 8.56$   $t h^{-1}$  (2022), and  $7.25 \pm 4.64$   $t h^{-1}$  (2023). The relatively low estimate in 2021 is primarily driven by an anomalously low value in October, when background  $XCH_4$  exceeded concentrations within the urban domain, resulting in near-zero or negative  $\Delta XCH_4$ . If



this month is excluded as a statistical outlier, the 2021 annual emission increases to  $10.11 \pm 6.28 \text{ t h}^{-1}$ , highlighting the sensitivity of the method to background characterization under weak enhancement conditions. The mean wind speed over the urban domain during 2021 to 2023 is  $5.15 \pm 0.55 \text{ m s}^{-1}$ , with pronounced seasonal variability (Fig. 4d). Comparison of Figs. 4b–d indicates that temporal variations in emission estimates are primarily controlled by variability in  $\Delta X\text{CH}_4$  rather than wind speed. Uncertainty propagation analysis attributes approximately 80% of the total emission uncertainty to variability in the methane enhancement, whereas wind-related uncertainty only accounts for about 20%. This result underscores that, for weakly enhanced urban regions (such as London), accurate background determination and robust enhancement retrievals are the dominant factors governing emission estimate reliability.

The bottom-up methane emissions for the London urban area, as reported by the EDGAR inventory, are shown in Fig. A1a. To ensure direct comparability with top-down estimates in this work, the gridded EDGAR emissions were extracted and summed over the same source box defined in Sect. 2.1.4. In this way, both bottom-up and satellite-based emissions refer to an identical spatial domain. The EDGAR-derived emissions are significantly lower than the satellite-based emission rates estimated using the improved source pixel method. Over the same spatial domain and time period, the top-down emission estimates in this work are approximately 2.1 times higher than the EDGAR inventory values. According to EDGAR, the dominant methane source in London during 2021–2023 is the landfills and waste, contributing on average approximately 63% of the total emissions (Fig. A3a). Fossil fuel-related emissions (e.g. leakage from natural gas transmission and distribution systems) represent the second largest source, accounting for about 32%, followed by agriculture activities (nearly 5% of total emission). Other sectors (e.g., wetlands and other anthropogenic sources) contribute comparatively smaller fractions.

### 3.2 Urban emissions in Los Angeles

Methane emissions over the Los Angeles urban area for the period 2021–2023 were estimated using the same improved source pixel method. The results are summarized in Fig. 5, along with the mask that delineates the source region. The spatial distribution of TROPOMI-derived  $X\text{CH}_4$  in Los Angeles city (Fig. 5a) reveals a pronounced methane hotspot over the defined urban domain, with clearly elevated concentrations relative to the surrounding background. In contrast to London, the methane enhancement over Los Angeles is spatially coherent and persistent, indicating a strong urban emission signal detectable from space. The three-year average emission estimate from 2021 to 2023 is  $47.19 \text{ t h}^{-1}$ , with a  $1 \sigma$  uncertainty range spanning from 13.51 to  $80.87 \text{ t h}^{-1}$ . As shown in Fig. 5b, the annual mean methane emissions increase from  $26.21 \pm 23.03 \text{ t h}^{-1}$  in 2021 to  $50.18 \pm 36.55 \text{ t h}^{-1}$  in 2022 and further to  $62.77 \pm 35.95 \text{ t h}^{-1}$  in 2023, indicating a substantial interannual growth over the study period. A clear seasonal pattern is apparent, with higher emission estimates generally occurring during winter and early spring. Notably, little to no valid emission estimates are available during the summer months, particularly in 2021 and 2023, likely due to persistent marine boundary layer clouds and coastal meteorological conditions that substantially reduce the number of usable satellite overpasses (e.g. insufficient valid pixels are available within either the source region or the upwind background region to satisfy the data quality thresholds defined in Sect. 2.1.1 and Sect. 2.3). Figures 5c and 5d show that the average methane enhancement  $\Delta X\text{CH}_4$  over the study period is  $10.66 \pm 5.87 \text{ ppb}$ , while the mean wind speed is  $2.96 \pm 1.10 \text{ m s}^{-1}$ . Although the seasonal variation of emission rate broadly follows that of  $\Delta X\text{CH}_4$ , uncertainty analysis in-

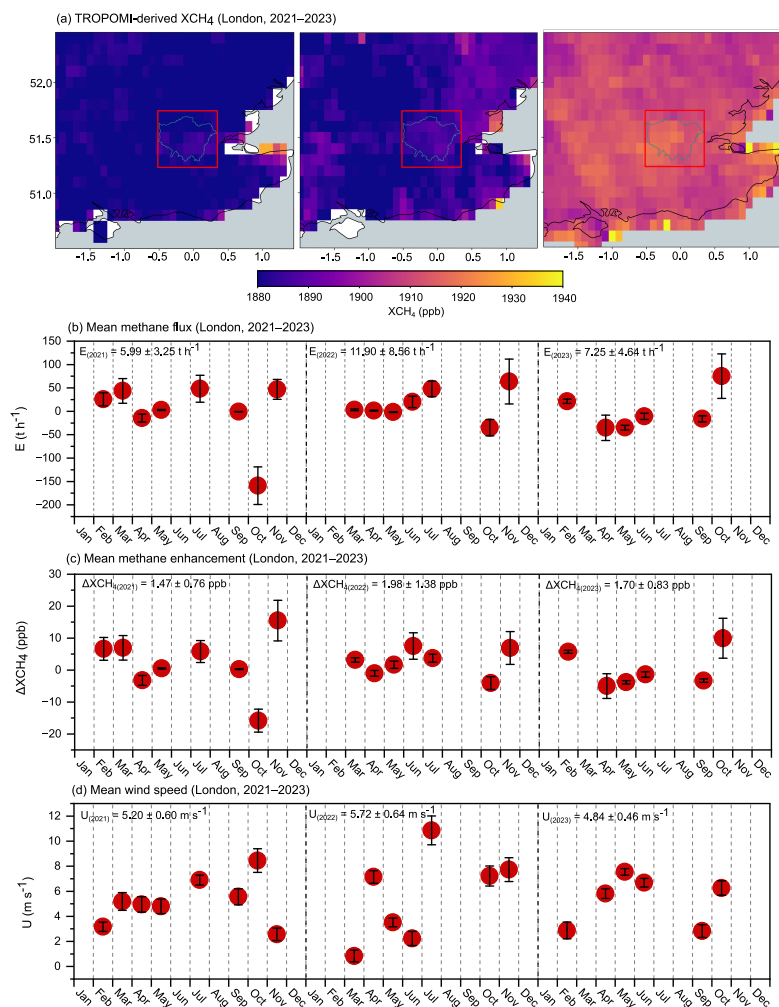


**Figure 4.** Results for the London urban area during 2021–2023. (a) Spatial distribution of TROPOMI-derived XCH<sub>4</sub>, with the defined source box outlined in red based on the blue administrative boundary. (b) Monthly mean methane emission rates derived using the improved source pixel method. (c) Mean methane enhancement. (d) Mean wind speed.

indicates that more than half of the total emission uncertainty is attributable to wind variability. This reflects the sensitivity of the emission rates calculation to wind speed during the satellite overpass window (19, 20, 21, 22 UTC), when coastal circulations and ocean–land breeze dynamics can induce substantial short-term wind fluctuations over the Los Angeles basin.

The spatial distribution of methane emissions from the EDGAR inventory for 2021–2023 is shown in Fig. A1b. When aggregated over the identical source domain used in the this work, the mean EDGAR emission for Los Angeles urban area is 20.07 t h<sup>-1</sup>, which is notably lower than the satellite-derived estimate of 47.19 ± 33.68 t h<sup>-1</sup>. Sectoral attribution (see Fig. A3b) indicates that Los Angeles is dominated by waste-related emissions, primarily from landfills, which account for more



than 90% of the total methane emissions in each study year. Fossil fuel-related sources represent a much smaller contribution, approximately 9% of the total.

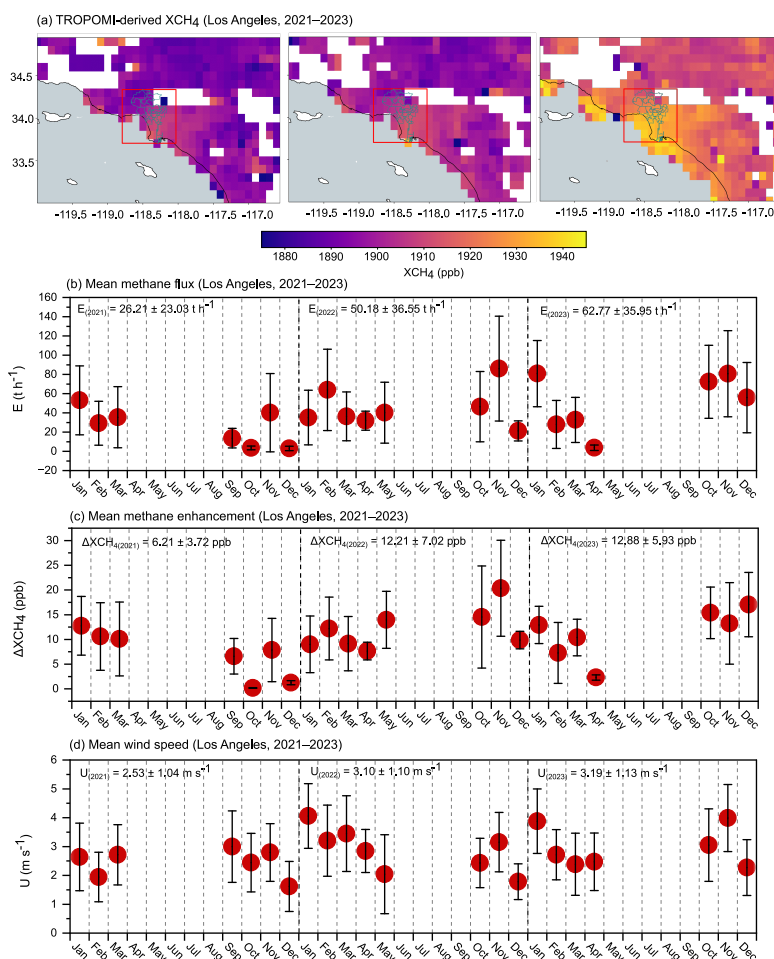


**Figure 5.** Results for the Los Angeles urban area during 2021–2023. (a) Spatial distribution of TROPOMI-derived XCH<sub>4</sub>, with the defined source region outlined in red based on the blue administrative boundary. (b) Monthly mean methane emission rate derived using the improved source pixel method. (c) Mean methane enhancement. (d) Mean wind speed.

### 345 3.3 Urban emissions in New York

New York serves as the third case study for evaluating the improved source pixel method. The corresponding results for 2021–2023 are summarized in Fig. 6. The TROPOMI-derived XCH<sub>4</sub> fields (Fig. 6a) exhibit a discernible enhancement over the defined urban domain, particularly in 2022 and 2023, indicating a persistent methane signal relative to the surrounding background. However, the geographic setting of New York—located at the confluence of major waterways and influenced by



350 frequent cloud cover—limits the number of valid satellite retrievals in certain months, especially during the 2021 and 2022. The temporal evolution of the derived methane emission rate is shown in Fig. 6b. The three-year mean emission is  $42.94 \text{ t h}^{-1}$  with a standard deviation of  $24.69 \text{ t h}^{-1}$ . Among the individual year, 2023 exhibits the highest annual mean emission rate ( $44.77 \pm 25.03 \text{ t h}^{-1}$ ), whereas 2022 shows the lowest ( $30.85 \pm 21.50 \text{ t h}^{-1}$ ). Monthly variability reveals a recurring seasonal structure, with relatively elevated emissions during early autumn, particularly in September. In contrast to the other two years, 355 2023 provides more continuous data coverage, with valid emission estimates available for most non-summer months. However, June–August remain largely data-limited, and intermittent gaps are still evident due to cloud contamination and quality-control filtering of satellite retrievals. Figures 6c and 6d indicate a mean methane enhancement of  $9.15 \pm 5.72 \text{ ppb}$  and an average wind speed of  $5.43 \pm 0.91 \text{ m s}^{-1}$  over the study period. Although seasonal variations in emission rates are primarily driven by changes in methane enhancement within the source region relative to the background, wind variability plays a non-negligible role in 360 modulating the magnitude of the calculated emissions. The relatively strong and seasonally variable winds over New York introduce additional variability during the satellite overpass window. Uncertainty analysis shows that methane enhancement accounts for approximately 60% of the total emission uncertainty, while wind contributes the remaining 40%, indicating a more balanced uncertainty structure compared to Los Angeles.

The spatial distribution of EDGAR gridded methane emissions for New York city is shown in Fig. A1c. Emissions within 365 the urban area are relatively weak and spatially diffuse, with only a few grid cells exhibiting moderate emission values. When aggregated over the identical source box used in this work (red box), the annual mean methane emission for the EDGAR inventory is  $4.38 \text{ t h}^{-1}$  for 2021–2023. This value is substantially lower than the satellite-derived estimate and corresponds to approximately 11% of the emission magnitude inferred from the improved source pixel method. Sectoral attribution indicates that emissions are dominated by waste-related sources (e.g. landfills and waste), contributing about 53% of the total, followed 370 closely by fossil fuel-related activities at approximately 45%. Other sectors represent only a minor fraction of the inventory-based emissions (Fig. A3c).

### 3.4 Comparison with inventories and previous studies

Figure 7 presents a comparison between our satellite-derived emission estimates based on improved source pixel method, three 375 widely used gridded bottom-up inventories, and five recently published top-down studies. Overall, our estimates consistently exceed the gridded inventory values across all three cities, ranging from 0.3 to 9.2 times higher than the publicly available EDGAR inventory. For London, comparison with the NAEI inventory indicates that bottom-up estimates generally underestimate urban methane emissions, with the exception of 2021, and the discrepancy reaches up to 45% in 2022. For the U.S. cities, the EPA inventory similarly reports lower emissions than our satellite-based results, with underestimations of approximately 56% for Los Angeles and 84% for New York.

380 The magnitude of city-scale methane emission estimates can vary substantially depending on how the urban domain is delineated, particularly when large point sources, such as landfills, are located along the urban fringe. These studies adopt different definitions of urban area and generally include contributions from nearly all source sectors. For example, Plant et al. (2022) and Nesser et al. (2024) quantify urban emissions based on the U.S. Census Bureau's Topologically Integrated Geographic

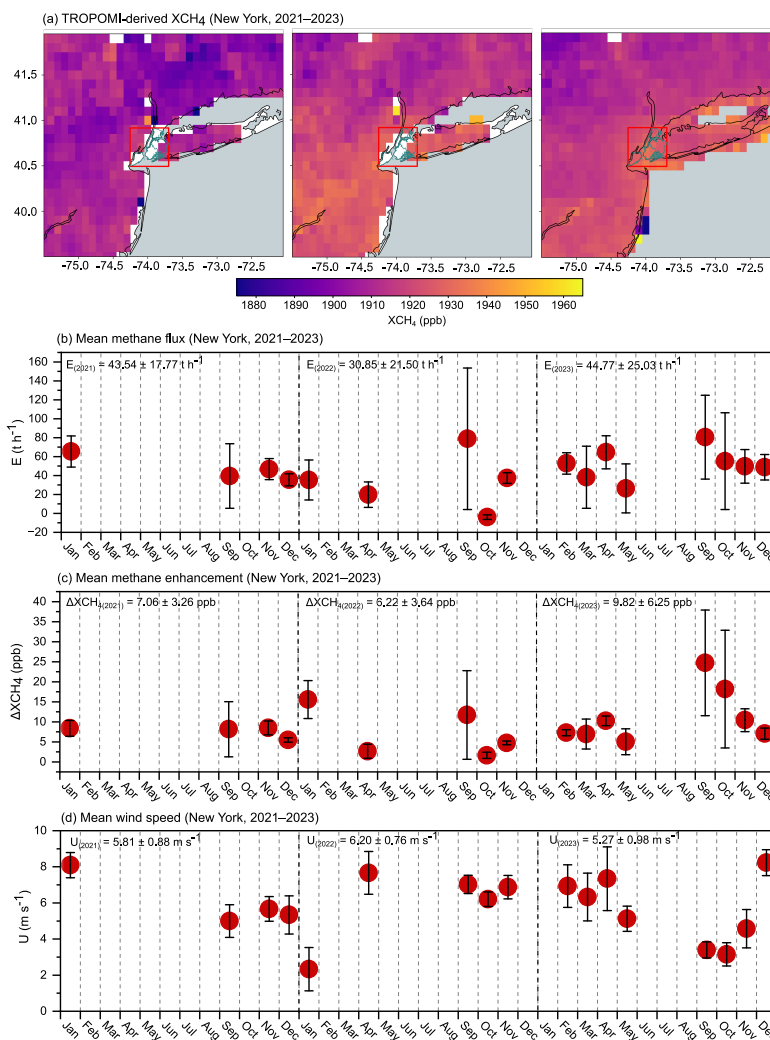


**Figure 6.** Results for the New York urban area during 2021-2023. (a) Spatial distribution of TROPOMI-derived XCH<sub>4</sub>, with the defined region outlined in red based on the administrative boundary (blue). (b) Monthly mean methane emission rate derived using the improved source pixel method. (c) Mean methane enhancement. (d) Mean wind speed.

385 Encoding and Referencing system (TIGER)/Line urban area definitions to standardize the spatial extent across the contiguous United States (CONUS) (U.S. Census Bureau, 2017). Most studies use aircraft measurements, tower observations or satellite retrievals combined with atmospheric chemical transport models to infer methane emissions (Nesser et al., 2024; Pitt et al., 2024; Yadav et al., 2023), while others use characteristic urban  $\Delta\text{CH}_4/\Delta\text{CO}$  enhancement ratios integrated with existing inventories to estimate methane emission rates (Plant et al., 2022). de Foy et al. (2023) applied a two-dimensional Gaussian model to estimate the local emissions required to reproduce the observed satellite retrievals.

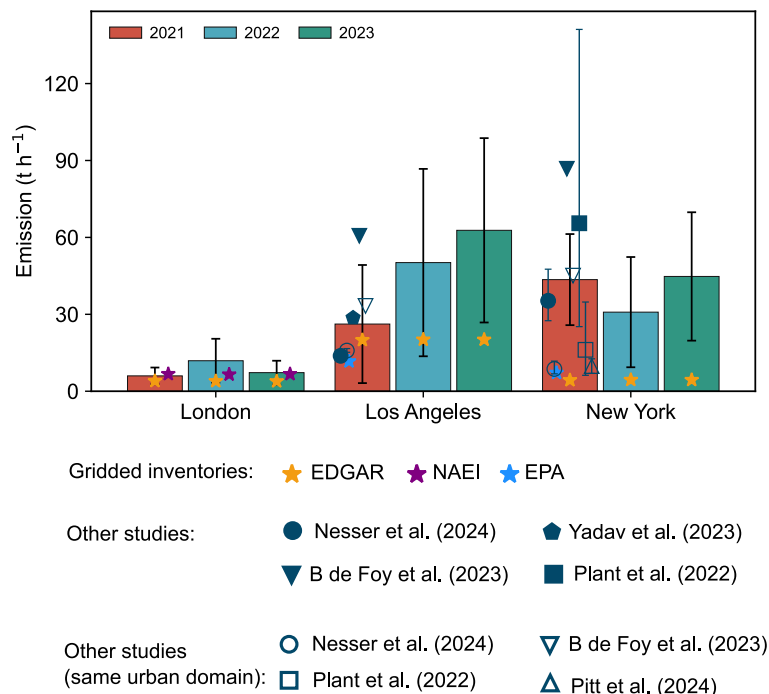


**Figure 7.** Comparison of annual methane emissions for the three case-study cities (2021-2023), including satellite-derived estimates based on improved source pixel method from this work, gridded bottom-up inventories, and previously published top-down studies.

390 We find generally lower, yet overall consistent, emission estimates when comparing our results for the three case studies with previous researches. This difference is likely attributable to the relatively strict urban domain defined in our study based on administrative boundaries, as well as the use of different emission quantification methods. To ensure spatial consistency in the comparison, we converted the reported emissions from previous studies into emission intensities (emission rate per unit area) and subsequently rescaled them to our defined urban domain. Yadav et al. (2023) reported a posterior estimate of  $28.65 \pm 0.55 \text{ t h}^{-1}$  based on sustained station observations for Los Angeles, which is very close to our estimate of  $26.21 \pm 23.03 \text{ t h}^{-1}$ . A study using TROPOMI observations to estimate methane emissions over U.S. urban areas reported substantially higher values of  $60.62 \text{ t h}^{-1}$  for Los Angeles and  $86.76 \text{ t h}^{-1}$  for New York (de Foy et al., 2023). However, after scaling their estimates to the same urban domain used in this work, these values decrease to  $33.27 \text{ t h}^{-1}$  and  $45.09 \text{ t h}^{-1}$ , respectively, which align well with our results. Plant et al. (2022) and Nesser et al. (2024) adopted the same U.S. Census urban area definition but applied

400 different emission quantification methods. They found different emission estimates for New York city, although the reported ranges largely overlap with the uncertainty bounds of our derived emissions. After scaling to the same urban domain, our estimated emission range remains consistent with the uncertainty reported by Plant et al. (2022), while remaining higher than the estimate from Nesser et al. (2024). For Los Angeles, although our study employs a different definition of urban boundary and a different emission quantification method, our estimates remain consistent with those of Nesser et al. (2024) under both



405 scaled and non-scaled conditions. Furthermore, Pitt et al. (2024) developed a high-resolution gridded inventory for New York  
city that is approximately 1.3 times larger than the EPA inventory by incorporating updated activity data, emission factors, and  
spatial proxies. Nevertheless, our emission estimate remains substantially higher when evaluated over the same gridded urban  
domain.

#### 4 Conclusions

410 This study presented a framework for monitoring, identifying, and quantifying urban methane emissions using TROPOMI  
retrievals in combination with an improved source pixel method. The methodological advancement lies in the incorporation  
of hourly resolved PBL-pressure weighted wind fields and an explicitly defined upwind background concentration. These  
refinements enhance the conceptual accuracy of the approach relative to the conventional source pixel method, which does  
not explicitly account for upwind background direction or the vertical structure of wind within PBL. The principal advantage  
415 of this method is that emissions can be inferred directly from satellite-observed methane enhancements over the elevated  
source region relative to their surrounding areas, along with a representative advective mean wind vector. We applied the  
improved method to TROPOMI observations over three major cities (London, Los Angeles, and New York) during 2021–2023  
to quantify orbit-level methane emissions and associated emission uncertainties. The satellite-derived estimates were further  
compared with widely used gridded bottom-up inventories and recently published top-down studies. Overall, our estimates  
420 consistently exceed the gridded inventory values across all three cities, although great inter-annual and inter-city variability is  
observed. When compared with previous top-down studies, the results show generally lower, yet overall consistent emission  
estimates. These differences can be partially attributed to variations in urban domain definitions and emission quantification  
methodologies. After rescaling study domains to ensure spatial consistency, our results largely fall within the uncertainty ranges  
reported in previous work.

425 Emission uncertainties in this study are typically on the order of tens of percent, comparable to those found by Buchwitz  
et al. (2017), who estimated relative uncertainties of about 50% for large emissions sources (i.e. several Mt CH<sub>4</sub> yr<sup>-1</sup>). A  
significant reason for this is that methane enhancement estimates are sensitive to background variability; however, when the  
signal over the urban area is proportionately larger than the surrounding background and background is less variable, the  
resulting emission uncertainty is significantly reduced. To reduce systematic uncertainties arising principally from cloud cover,  
430 heterogeneous albedo of coast pixels, and aerosol scattering, we retained only high-quality XCH<sub>4</sub> retrievals under cloud-free  
conditions and applied strict filtering criteria (Sect. 2.1) to exclude pixels with poor spectral fits and other retrieval artifacts.  
Additional filtering thresholds were introduced in the final emission estimates to minimize the influence of limited sampling  
and potential outliers that passed earlier constraints. These stringent filtering criteria inevitably resulted in the exclusion of a  
substantial fraction of satellite overpasses, representing a key limitation of the method used in this work. The reduced data  
435 coverage may introduce biases in the inferred seasonal and inter-annual variability. However, we argue that this trade-off  
is necessary to preserve statistical reliability and avoid systematic overestimation or underestimation of emissions. These  
considerations highlight the importance of understanding how such biases may manifest when comparing annualized emissions



440 derived from the source pixel method using satellite retrievals. Our results provide evidence that satellite observations can serve as a promising technology for ongoing city-scale emission detection, reconciliation, and reporting through long-term global monitoring, which helps build methane emission characteristics and track whether emission targets are being met.

*Code availability.* The code used in this study is available from the corresponding author upon request.

*Data availability.* The TROPOMI methane retrieval products for 2021–2023 are available at <https://browser.dataspace.copernicus.eu/>. ERA5 hourly-resolved wind fields from the European Centre for Medium-Range Weather Forecasts (ECMWF), used to calculate the pressure-weighted mean wind over the source region within the planetary boundary layer (PBL), can be accessed at <https://cds.climate.copernicus.eu/datasets/reanalysis-era5-pressure-levels?tab=download>. Anthropogenic methane emissions from the EDGAR inventory are available at [https://edgar.jrc.ec.europa.eu/dataset\\_ghg2024](https://edgar.jrc.ec.europa.eu/dataset_ghg2024). WetCHARTs wetland methane emissions can be obtained from <https://www.earthdata.nasa.gov/data/catalog/ornl-cloud-monthlywetland-ch4-wetchartsv2-2346-1.3.3>. The NAEI emission datasets are available at <https://naei.energysecurity.gov.uk/data/maps>. The EPA emission datasets can be accessed at <https://zenodo.org/records/8367082>.

## Appendix A

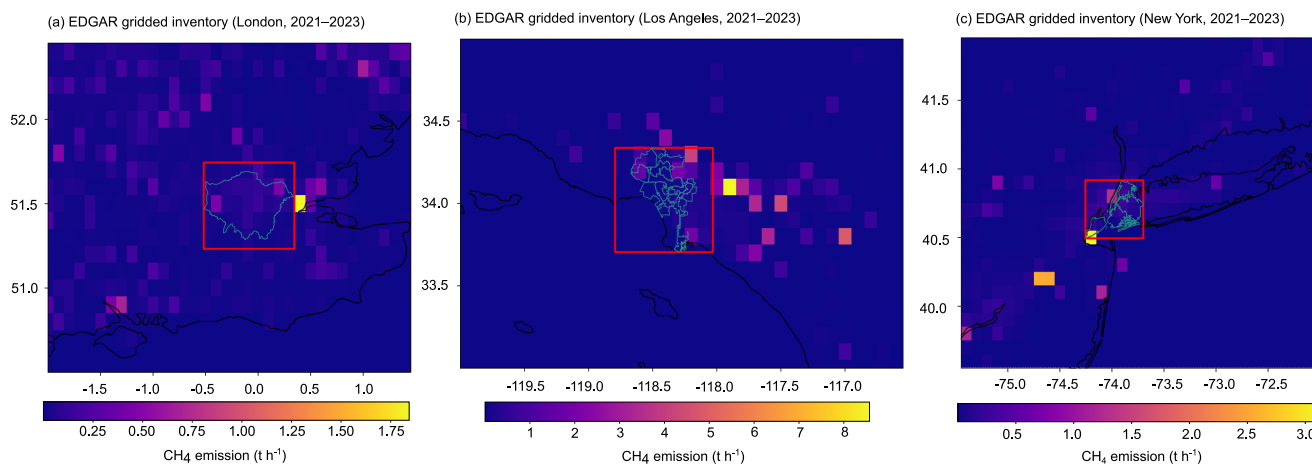


**Figure A1.** Annual average of emission inventories from EDGAR datasets for London (a), Los Angeles (b) and New York (c) from 2021 to 2023.

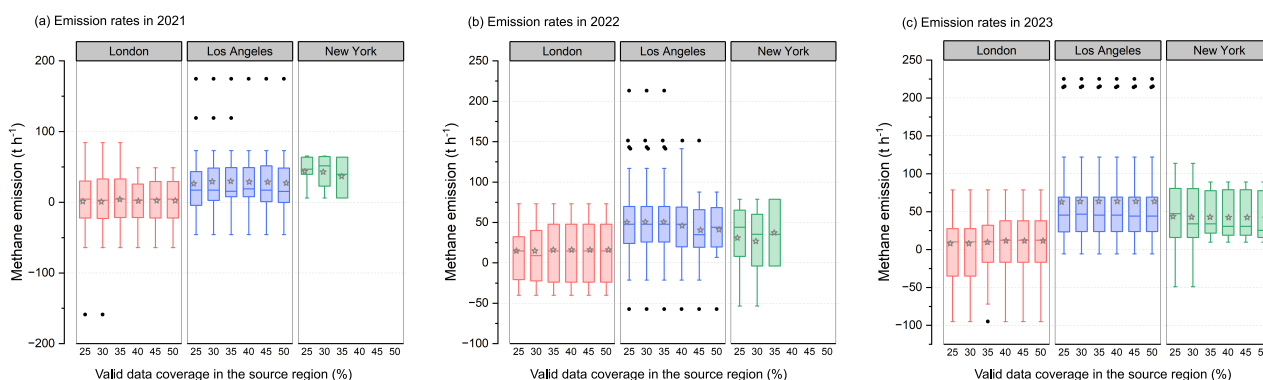


**Figure A2.** Sensitivity of emission rates in three case study cities to populated valid data coverage in the source region after filtering, shown for (a) 2021, (b) 2022, and (c) 2023.

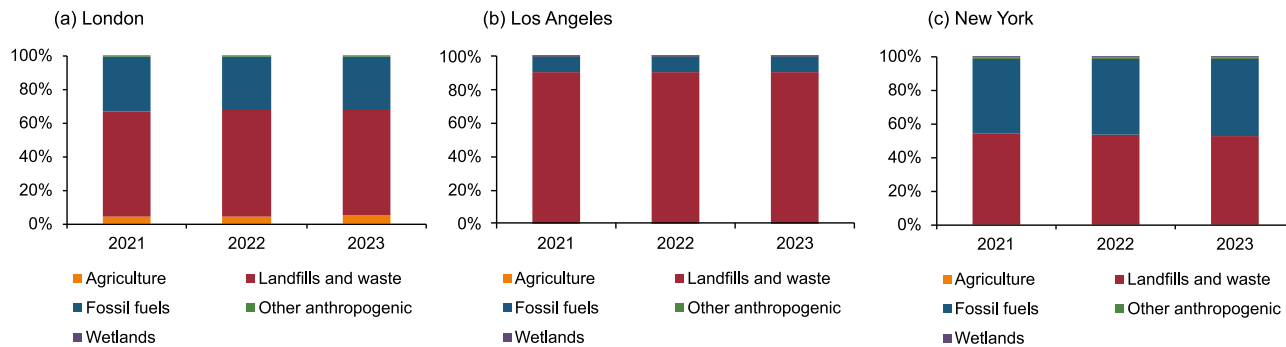


**Figure A3.** Fractions of four major aggregated emission sectors from EDGAR inventory and natural wetland emissions from WetCHARTs in (a) London, (b) Los Angeles, and (c) New York.



450 *Author contributions.* HL and GA designed the paper and analyzed the results. HL performed all the calculations and visualized the results. The Python codes for estimating methane emissions and uncertainties were developed by HL. GA supervised the research. MT, and HR provided helpful suggestion during the data acquisition and filtering process. All co-authors contributed to the manuscript review.

*Competing interests.* The contact author has declared that none of the authors has any competing interests.

*Acknowledgements.* AI tools (such as ChatGPT) were used for light language editing of this manuscript and for code assistance. All AI-  
455 assisted language and code outputs were reviewed and verified by the authors.

*Financial support.* This research has been supported by the Dean's Doctoral Scholarship from the University of Manchester.



## References

- Allen, G., Hollingsworth, P., Kabbabe, K., Pitt, J. R., Mead, M. I., Illingworth, S., Roberts, G., Bourn, M., Shallcross, D. E., and Percival, C. J.: The development and trial of an unmanned aerial system for the measurement of methane flux from landfill and greenhouse gas emission hotspots, *Waste Management*, 87, 883–892, <https://doi.org/10.1016/j.wasman.2017.12.024>, 2019.
- 460 Anderson, D. C., Lindsay, A., DeCarlo, P. F., and Wood, E. C.: Urban emissions of nitrogen oxides, carbon monoxide, and methane determined from ground-based measurements in Philadelphia, *Environmental science & technology*, 55, 4532–4541, <https://doi.org/10.1021/acs.est.1c00294>, 2021.
- Balagus, N., Jacob, D. J., Lorente, A., Maasakkers, J. D., Parker, R. J., Boesch, H., Chen, Z., Kelp, M. M., Nesser, H., and Varon, D. J.: A blended TROPOMI+ GOSAT satellite data product for atmospheric methane using machine learning to correct retrieval biases, *Atmospheric Measurement Techniques*, 16, 3787–3807, <https://doi.org/10.5194/amt-16-3787-2023>, 2023.
- 465 Bloom, A. A., Bowman, K. W., Lee, M., Turner, A. J., Schroeder, R., Worden, J. R., Weidner, R. J., McDonald, K. C., and Jacob, D. J.: CMS: Global 0.5-deg Wetland Methane Emissions and Uncertainty (WetCHARTs v1.3.3), ORNL DAAC, Oak Ridge, Tennessee, USA, <https://doi.org/10.3334/ORNLDAAC/2346>, 2024.
- 470 Buchwitz, M., Schneising, O., Reuter, M., Heymann, J., Krautwurst, S., Bovensmann, H., Burrows, J. P., Boesch, H., Parker, R. J., Somkuti, P., et al.: Satellite-derived methane hotspot emission estimates using a fast data-driven method, *Atmospheric Chemistry and Physics*, 17, 5751–5774, <https://doi.org/10.5194/acp-17-5751-2017>, 2017.
- Butz, A., Guerlet, S., Hasekamp, O., Schepers, D., Galli, A., Aben, I., Frankenberg, C., Hartmann, J.-M., Tran, H., Kuze, A., et al.: Toward accurate CO<sub>2</sub> and CH<sub>4</sub> observations from GOSAT, *Geophysical Research Letters*, 38, <https://doi.org/10.1029/2011GL047888>, 2011.
- 475 City of Los Angeles: City Boundary Dataset, <https://geohub.lacity.org/datasets/lahub::city-boundary/explore>, accessed: 2026-02-12, 2026.
- Cooper, J., Dubey, L., and Hawkes, A.: Methane detection and quantification in the upstream oil and gas sector: the role of satellites in emissions detection, reconciling and reporting, *Environmental Science: Atmospheres*, 2, 9–23, <https://doi.org/10.1039/D1EA00046B>, 2022.
- Crippa, M., Guizzardi, D., Pagani, F., Schiavina, M., Melchiorri, M., Pisoni, E., Graziosi, F., Muntean, M., Maes, J., Dijkstra, L., et al.: Insights into the spatial distribution of global, national, and subnational greenhouse gas emissions in the Emissions Database for Global Atmospheric Research (EDGAR v8.0), *Earth System Science Data*, 16, 2811–2830, <https://doi.org/10.5194/essd-16-2811-2024>, 2024.
- de Foy, B., Schauer, J. J., Lorente, A., and Borsdorff, T.: Investigating high methane emissions from urban areas detected by TROPOMI and their association with untreated wastewater, *Environmental Research Letters*, 18, 044004, <https://doi.org/10.1088/1748-9326/acc118>, 2023.
- 485 Defratyka, S. M., Paris, J.-D., Yver-Kwok, C., Fernandez, J. M., Korben, P., and Bousquet, P.: Mapping urban methane sources in Paris, France, *Environmental science & technology*, 55, 8583–8591, <https://doi.org/10.1021/acs.est.1c00859>, 2021.
- Forster, P., Storelvmo, T., Armour, K., Collins, W., Dufresne, J.-L., Frame, D., Lunt, D. J., Mauritsen, T., Palmer, M. D., Watanabe, M., Wild, M., and Zhang, H.: The Earth's Energy Budget, Climate Feedbacks and Climate Sensitivity, in: *Climate Change 2021 – The Physical Science Basis: Working Group I Contribution to the Sixth Assessment Report of the Intergovernmental Panel on Climate Change*, pp. 923–1054, Cambridge University Press, <https://doi.org/10.1017/9781009157896.009>, 2021.
- 490 Global Methane Pledge: Global Methane Pledge website: Pledges, <https://globalmethanepledge.ccacoalition.org/#pledges>, last access: 22 September 2025, 1 September, 2023.



- Greater London Authority: Night Time Observatory: GIS Boundaries, <https://data.london.gov.uk/night-time-observatory/gis-boundaries/>, accessed: 2026-02-12, 2026.
- 495 Hasekamp, O., Lorente, A., Hu, H., Butz, A., Aan de Brugh, J., and Landgraf, J.: Algorithm Theoretical Baseline Document for Sentinel-5 Precursor Methane Retrieval, SRON-S5P-LEV2-RP-001 CI-7430-ATBD, SRON Netherlands Institute for Space Research, [https://sentiwiki.copernicus.eu/\\_\\_attachments/1673595/SRON-S5P-LEV2-RP-001%20-%20Sentinel-5P%20TROPOMI%20ATBD%20Methane%20retrieval%202024%20-%202.8.0.pdf?inst-v=eab10fa0-1887-4666-8d61-93ebcf449302](https://sentiwiki.copernicus.eu/__attachments/1673595/SRON-S5P-LEV2-RP-001%20-%20Sentinel-5P%20TROPOMI%20ATBD%20Methane%20retrieval%202024%20-%202.8.0.pdf?inst-v=eab10fa0-1887-4666-8d61-93ebcf449302), version 2.8.0, released 13 November 2024, 2024.
- 500 He, L., Zeng, Z.-C., Pongetti, T. J., Wong, C., Liang, J., Gurney, K. R., Newman, S., Yadav, V., Verhulst, K., Miller, C. E., et al.: Atmospheric methane emissions correlate with natural gas consumption from residential and commercial sectors in Los Angeles, *Geophysical Research Letters*, 46, 8563–8571, <https://doi.org/10.1029/2019GL083400>, 2019.
- Helfter, C., Tremper, A. H., Halios, C. H., Kotthaus, S., Borgeggen, A., Grimmond, C. S. B., Barlow, J. F., and Nemitz, E.: Spatial and temporal variability of urban fluxes of methane, carbon monoxide and carbon dioxide above London, UK, *Atmospheric Chemistry and Physics*, 16, 10 543–10 557, <https://doi.org/10.5194/acp-16-10543-2016>, 2016.
- 505 Hersbach, H., Bell, B., Berrisford, P., Hirahara, S., Horányi, A., Muñoz-Sabater, J., Nicolas, J., Peubey, C., Radu, R., Schepers, D., et al.: The ERA5 global reanalysis, *Quarterly journal of the royal meteorological society*, 146, 1999–2049, <https://doi.org/10.1002/qj.3803>, 2020.
- Hu, H., Landgraf, J., Detmers, R., Borsdorff, T., Aan de Brugh, J., Aben, I., Butz, A., and Hasekamp, O.: Toward global mapping of methane with TROPOMI: First results and intersatellite comparison to GOSAT, *Geophysical Research Letters*, 45, 3682–3689, <https://doi.org/10.1002/2018gl077259>, 2018.
- 510 IPCC: Climate Change 2023: Synthesis Report, Summary for Policymakers. Contribution of Working Groups I, II and III to the Sixth Assessment Report of the Intergovernmental Panel on Climate Change, Tech. rep., Intergovernmental Panel on Climate Change, Geneva, Switzerland, <https://doi.org/10.59327/IPCC/AR6-9789291691647>, 2023.
- Jacob, D. J., Turner, A. J., Maasackers, J. D., Sheng, J., Sun, K., Liu, X., Chance, K., Aben, I., McKeever, J., and Frankenberg, C.: Satellite observations of atmospheric methane and their value for quantifying methane emissions, *Atmospheric Chemistry and Physics*, 16, 14 371–14 396, <https://doi.org/10.5194/acp-16-14371-2016>, 2016.
- 515 Liu, M., van der A, R., van Weele, M., Bryan, L., Eskes, H., Veeffkind, P., Liu, Y., Lin, X., de Laat, J., and Ding, J.: Current potential of CH<sub>4</sub> emission estimates using TROPOMI in the Middle East, *Atmospheric Measurement Techniques*, 17, 5261–5277, <https://doi.org/10.5194/amt-17-5261-2024>, 2024.
- 520 Maasackers, J. D., McDuffie, E. E., Sulprizio, M. P., Chen, C., Schultz, M., Brunelle, L., Thrush, R., Steller, J., Sherry, C., Jacob, D. J., et al.: A gridded inventory of annual 2012–2018 US anthropogenic methane emissions, *Environmental science & technology*, 57, 16 276–16 288, <https://doi.org/10.1021/acs.est.3c05138>, 2023.
- Maazallahi, H., Fernandez, J. M., Menoud, M., Zavala-Araiza, D., Weller, Z. D., Schwietzke, S., Von Fischer, J. C., Denier Van Der Gon, H., and Röckmann, T.: Methane mapping, emission quantification, and attribution in two European cities: Utrecht (NL) and Hamburg (DE), *Atmospheric Chemistry and Physics*, 20, 14 717–14 740, <https://doi.org/10.5194/acp-20-14717-2020>, 2020.
- 525 Nesser, H., Jacob, D. J., Maasackers, J. D., Lorente, A., Chen, Z., Lu, X., Shen, L., Qu, Z., Sulprizio, M. P., Winter, M., et al.: High-resolution US methane emissions inferred from an inversion of 2019 TROPOMI satellite data: contributions from individual states, urban areas, and landfills, *Atmospheric Chemistry and Physics*, 24, 5069–5091, <https://doi.org/10.5194/acp-24-5069-2024>, 2024.
- New York State GIS Program Office: Civil Boundaries, <https://gis.ny.gov/civil-boundaries>, accessed: 2026-02-12, 2026.



- 530 Pandey, S., Houweling, S., Lorente, A., Borsdorff, T., Tsvilidou, M., Bloom, A. A., Poulter, B., Zhang, Z., and Aben, I.: Using satellite data to identify the methane emission controls of South Sudan's wetlands, *Biogeosciences*, 18, 557–572, <https://doi.org/10.5194/bg-18-557-2021>, 2021.
- Pitt, J. R., Allen, G., Bauguitte, S. J.-B., Gallagher, M. W., Lee, J. D., Drysdale, W., Nelson, B., Manning, A. J., and Palmer, P. I.: Assessing London CO<sub>2</sub>, CH<sub>4</sub> and CO emissions using aircraft measurements and dispersion modelling, *Atmospheric Chemistry and Physics*, 19, 8931–8945, <https://doi.org/10.5194/acp-19-8931-2019>, 2019.
- 535 Pitt, J. R., Lopez-Coto, I., Hajny, K. D., Tomlin, J., Kaeser, R., Jayarathne, T., Stirm, B. H., Floerchinger, C. R., Loughner, C. P., Gately, C. K., et al.: New York City greenhouse gas emissions estimated with inverse modeling of aircraft measurements, *Elementa: Science of the Anthropocene*, 10, 00082, <https://doi.org/10.1525/elementa.2021.00082>, 2022.
- Pitt, J. R., Lopez-Coto, I., Karion, A., Hajny, K. D., Tomlin, J., Kaeser, R., Jayarathne, T., Stirm, B. H., Floerchinger, C. R., Loughner, C. P., et al.: Underestimation of thermogenic methane emissions in New York City, *Environmental Science & Technology*, 58, 9147–9157, <https://doi.org/10.1021/acs.est.3c10307>, 2024.
- 540 Plant, G., Kort, E. A., Floerchinger, C., Gvakharia, A., Vimont, I., and Sweeney, C.: Large fugitive methane emissions from urban centers along the US East Coast, *Geophysical research letters*, 46, 8500–8507, <https://doi.org/10.1029/2019GL082635>, 2019.
- Plant, G., Kort, E. A., Murray, L. T., Maasackers, J. D., and Aben, I.: Evaluating urban methane emissions from space using TROPOMI methane and carbon monoxide observations, *Remote Sensing of Environment*, 268, 112756, <https://doi.org/10.1016/j.rse.2021.112756>, 2022.
- 545 Prather, M. J., Holmes, C. D., and Hsu, J.: Reactive greenhouse gas scenarios: Systematic exploration of uncertainties and the role of atmospheric chemistry, *Geophysical Research Letters*, 39, L09803, <https://doi.org/10.1029/2012GL051440>, 2012.
- Saint-Vincent, P. M. and Pekney, N. J.: Beyond-the-meter: Unaccounted sources of methane emissions in the natural gas distribution sector, *Environmental science & technology*, 54, 39–49, <https://doi.org/10.1021/acs.est.9b04657>, 2019.
- 550 Saunio, M., Bousquet, P., Poulter, B., Peregón, A., Ciais, P., Canadell, J. G., Dlugokencky, E. J., Etiope, G., Bastviken, D., Houweling, S., et al.: Variability and quasi-decadal changes in the methane budget over the period 2000–2012, *Atmospheric Chemistry and Physics*, 17, 11135–11161, <https://doi.org/10.5194/acp-17-11135-2017>, 2017.
- Saunio, M., Martinez, A., Poulter, B., Zhang, Z., Raymond, P. A., Regnier, P., Canadell, J. G., Jackson, R. B., Patra, P. K., Bousquet, P., et al.: Global methane budget 2000–2020, *Earth System Science Data*, 17, 1873–1958, <https://doi.org/10.5194/essd-17-1873-2025>, 2025.
- 555 Schiferl, L. D., Hallward-Driemeier, A., Zhao, Y., Toledo-Crow, R., and Commane, R.: Missing wintertime methane emissions from New York City related to combustion, *Atmospheric Chemistry and Physics*, 25, 15683–15700, <https://doi.org/10.5194/acp-25-15683-2025>, 2025.
- Schneising, O., Buchwitz, M., Hachmeister, J., Vanselow, S., Reuter, M., Buschmann, M., Bovensmann, H., and Burrows, J. P.: Advances in retrieving XCH<sub>4</sub> and XCO from Sentinel-5 Precursor: improvements in the scientific TROPOMI/WFMD algorithm, *Atmospheric Measurement Techniques*, 16, 669–694, <https://doi.org/10.5194/amt-16-669-2023>, 2023.
- 560 Shen, L., Jacob, D. J., Gautam, R., Omara, M., Scarpelli, T. R., Lorente, A., Zavala-Araiza, D., Lu, X., Chen, Z., and Lin, J.: National quantifications of methane emissions from fuel exploitation using high resolution inversions of satellite observations, *Nature Communications*, 14, 4948, <https://doi.org/10.1038/s41467-023-40671-6>, 2023.
- 565 Sicsik-Paré, A., Fortems-Cheiney, A., Pison, I., Broquet, G., Opler, A., Potier, E., Martinez, A., Schneising, O., Buchwitz, M., Maasackers, J. D., et al.: Can we obtain consistent estimates of the emissions in Europe from three different CH<sub>4</sub> TROPOMI products?, *EGUsphere*, 2025, 1–48, <https://doi.org/10.5194/egusphere-2025-2622>, 2025.



- Szopa, S., Naik, V., Adhikary, B., Artaxo, P., Bernsten, T., Collins, W., Fuzzi, S., Gallardo, L., Kiendler-Scharr, A., Klimont, Z., Liao, H., Unger, N., and Zanis, P.: Short-lived Climate Forcers, in: *Climate Change 2021: The Physical Science Basis*, edited by Masson-Delmotte, V., Zhai, P., Pirani, A., Connors, S., Péan, C., Berger, S., Caud, N., Chen, Y., Goldfarb, L., Gomis, M., Huang, M., Leitzell, K., Lonnoy, E., Matthews, J., Maycock, T., Waterfield, T., Yelekçi, O., Yu, R., and Zhou, B., pp. 817–922, Cambridge University Press, Cambridge, UK and New York, NY, USA, <https://doi.org/10.1017/9781009157896.008>, 2021.
- Tibrewal, K., Ciais, P., Saunois, M., Martinez, A., Lin, X., Thanwerdas, J., Deng, Z., Chevallier, F., Giron, C., Albergel, C., et al.: Assessment of methane emissions from oil, gas and coal sectors across inventories and atmospheric inversions, *Communications Earth & Environment*, 5, 26, <https://doi.org/10.1038/s43247-023-01190-w>, 2024.
- Tsagatakis, I., Richardson, J., Evangelides, C., Hows, S.-M., Hamilton, N., Richmond, B., Pearson, B., Passant, N., Pommier, M., Pizzolato, M., and Otto, A.: UK Spatial Emissions Methodology: A report of the National Atmospheric Emission Inventory 2022, Tech. rep., National Atmospheric Emission Inventory, retrieved from <https://naei.energysecurity.gov.uk/reports/uk-spatial-emissions-methodology-report-national-atmosphericemission-inventory-2022>, 2024.
- United Nations Department of Economic and Social Affairs: The Sustainable Development Goals Report 2025, Tech. rep., United Nations Department of Economic and Social Affairs, New York, <https://unstats.un.org/sdgs/report/2025/>, revision August 2025, 2025.
- U.S. Census Bureau: TIGER/Line Shapefile, 2017, 2010 Nation, U.S., 2010 Census Urban Area National, U.S. Census Bureau data set, <https://catalog.data.gov/dataset/tiger-line-shapefile-2017-2010-nation-u-s-2010-census-urban-area-national>, 2017.
- U.S. Environmental Protection Agency: Global Non-CO<sub>2</sub> Greenhouse Gas Emission Projections & Mitigation Potential: 2015–2050, Tech. Rep. EPA-430-R-19-010, U.S. Environmental Protection Agency, [https://www.epa.gov/sites/default/files/2019-09/documents/epa\\_non-co2\\_greenhouse\\_gases\\_rpt-epa430r19010.pdf](https://www.epa.gov/sites/default/files/2019-09/documents/epa_non-co2_greenhouse_gases_rpt-epa430r19010.pdf), 2019.
- Vanselow, S., Schneising, O., Buchwitz, M., Reuter, M., Bovensmann, H., Boesch, H., and Burrows, J. P.: Automated detection of regions with persistently enhanced methane concentrations using Sentinel-5 Precursor satellite data, *Atmospheric Chemistry and Physics*, 24, 10 441–10 473, <https://doi.org/10.5194/acp-24-10441-2024>, 2024.
- Varon, D. J., Jacob, D. J., McKeever, J., Jervis, D., Durak, B. O., Xia, Y., and Huang, Y.: Quantifying methane point sources from fine-scale satellite observations of atmospheric methane plumes, *Atmospheric Measurement Techniques*, 11, 5673–5686, <https://doi.org/10.5194/amt-11-5673-2018>, 2018.
- Veefkind, J. P., Aben, I., McMullan, K., Förster, H., De Vries, J., Otter, G., Claas, J., Eskes, H., De Haan, J., Kleipool, Q., et al.: TROPOMI on the ESA Sentinel-5 Precursor: A GMES mission for global observations of the atmospheric composition for climate, air quality and ozone layer applications, *Remote sensing of environment*, 120, 70–83, <https://doi.org/10.1016/j.rse.2011.09.027>, 2012.
- Wang, X., Jacob, D. J., Nesser, H., Balasus, N., Estrada, L. A., Sulprizio, M. P., Cusworth, D. H., Scarpelli, T. R., Chen, Z., East, J. D., et al.: Quantifying urban and landfill methane emissions in the United States using TROPOMI satellite data, *Science Advances*, 12, eadz9308, <https://doi.org/10.1126/sciadv.adz9308>, 2026.
- Weller, Z. D., Hamburg, S. P., and von Fischer, J. C.: A national estimate of methane leakage from pipeline mains in natural gas local distribution systems, *Environmental science & technology*, 54, 8958–8967, <https://doi.org/10.1021/acs.est.0c00437>, 2020.
- Xing, Z., Hugenholtz, C., Barchyn, T. E., and Vollrath, C.: Satellite observations indicate a declining trend of methane emissions from heavy oil production in Canada, *Environmental Science & Technology Letters*, 12, 1334–1339, <https://doi.org/10.1021/acs.estlett.5c00426>, 2025.
- Yadav, V., Verhulst, K., Duren, R., Thorpe, A., Kim, J., Keeling, R., Weiss, R., Cusworth, D., Mountain, M., Miller, C., et al.: A declining trend of methane emissions in the Los Angeles basin from 2015 to 2020, *Environmental Research Letters*, 18, 034004, <https://doi.org/10.1088/1748-9326/acb6a9>, 2023.

<https://doi.org/10.5194/egusphere-2026-2570>

Preprint. Discussion started: 20 May 2026

© Author(s) 2026. CC BY 4.0 License.



Zhu, L., Jacob, D. J., Keutsch, F. N., Mickley, L. J., Scheffe, R., Strum, M., González Abad, G., Chance, K., Yang, K., Rappenglück, B., et al.: Formaldehyde (HCHO) as a hazardous air pollutant: Mapping surface air concentrations from satellite and inferring cancer risks in the United States, *Environmental Science & Technology*, 51, 5650–5657, <https://doi.org/10.1021/acs.est.7b01356>, 2017.